Remote sensing ice supersaturation inside and near cirrusclouds: a case study in the subtropics

Christophe Hoareau, Vincent Noël, Hélène Chepfer, Jérôme Vidot, Marjolaine Chiriaco, Sophie Bastin, Mathieu Reverdy, Gregory Cesana

ATMOSPHERIC SCIENCE LETTERS
Atmos. Sci. Let. **17**: 639–645 (2016)
Published online in Wiley Online Library
(wileyonlinelibrary.com) **DOI:** 10.1002/asl.714

RMetS
Royal Meteorological Society

Remote sensing ice supersaturation inside and near cirrus clouds: a case study in the subtropics

C. Hoareau,[1] V. Noel,[2,*] H. Chepfer,[3] J. Vidot,[4] M. Chiriaco,[5] S. Bastin,[5] M. Reverdy[6] and G. Cesana[7]

[1]*CNRS, Laboratoire de Météorologie Dynamique, UMR 8539, Palaiseau, France*
[2]*CNRS, Laboratoire d'Aérologie, UMR 5560, Toulouse, France*
[3]*UPMC, Laboratoire de Météorologie Dynamique, UMR 8539, Palaiseau, France*
[4]*Météo-France, Centre de Météorologie Spatiale de, Lannion Cedex, France*
[5]*Université Versailles St-Quentin, Sorbonne Universités, UPMC Univ. Paris 06; CNRS/INSU, LATMOS-IPSL, 11 bd d'Alembert, Guyancourt, France*
[6]*FX-Conseil, Laboratoire de Météorologie Dynamique, UMR 8539, Palaiseau, France*
[7]*Jet Propulsion Laboratory, California Institute of Technology, Pasadena, CA, USA*

**Correspondence to:*
V. Noel, CNRS, Laboratoire d'Aérologie, 14 Avenue Edouard Belin, 31400 Toulouse, France.
E-mail: vincent.noel@aero.obs-mip.fr

Received: 13 November 2015
Revised: 14 October 2016
Accepted: 18 October 2016

Abstract

Combining vertically resolved lidar retrievals of water vapor and cloud detection, we document a 2-day subtropical cirrus case study over La Réunion (20.9°S–55.5°E) in March 2005, focusing on the conditions of ice supersaturation inside and near the observed cloud. Using satellite observations, we describe the synoptic conditions leading to cloud formation. Supersaturation occurs 25% of the time within the cirrus, up to 35% in its middle segment, where relative humidity goes beyond 150%. In clear-sky areas, relative humidity stays consistently low, especially in profiles without clouds. High-troposphere atmospheric waves could initiate the formation of supersaturation conditions, especially on 16 March.

Keywords: **cirrus; water vapor; supersaturation; Raman lidar; subtropics**

1. Introduction

Cirrus clouds form mostly at temperatures colder than 240 K and altitudes higher than 7 km (Heintzenberg and Charlson, 2009). Optically thin cirrus modulate the Earth radiative budget mainly through their long-wave radiative warming effect due to their cold temperatures. Complex interactions between dynamical, microphysical and radiative processes drive their formation and evolution (Dinh and Fueglistaler, 2014). Those are controlled, on first approximation, by the temperature and amount of humidity available in the environment: the relative humidity over ice crossing 100%, or supersaturation. During cloud formation, gas phase water is depleted through ice crystal growth. Supersaturation, however, can persist in formed cirrus clouds, as shown by *in situ* observations (Krämer *et al.*, 2009, Jensen *et al.*, 2013) and models (Spichtinger and Gierens, 2009; Spitchinger and Cziczo, 2010). Documenting the responsible processes requires access to fine temporal and spatial changes during the entire cloud life cycle. Fine-scale aircraft observations have provided relevant cutting-edge information (e.g. Gayet *et al.*, 2004; Spichtinger *et al.*, 2004), but because their autonomy is limited aircraft cannot document all synoptic conditions everywhere on the globe. Moreover, they can hardly document the lifetime of a cloud system over several days. Satellites observations are global (Sandor *et al.*, 2000; Lamquin *et al.*, 2009; Su *et al.*, 2009; Martins *et al.*, 2011; Reverdy *et al.*, 2012) but have coarse spatiotemporal resolutions not suited to the small-scale processes considered here. Ground-based observation, if limited in space, can provide several days of observations at high spatiotemporal resolution.

The difficulty to document the processes responsible for the persistence of supersaturation at a large-scale contributes to a poor representation of cirrus clouds in climate models (Zhang *et al.*, 2005; Ringer *et al.*, 2006). Models often overestimate the cirrus cloud amount (Nam and Quaas, 2012), put the top of deep convective clouds in the Tropics ±2 km away from the observed 16 km (Cesana and Chepfer, 2012), and overestimate the occurrence of ice clouds by up to 20% in the Tropics between −60 and −20 °C (Delanoë *et al.*, 2011). To better model cirrus clouds formation and dissipation, a prognostic treatment of cloud fraction, humidity and ice is required that explicitly takes into account their subgrid-scale variability (Kärcher and Burkhardt, 2008). Although some global models now allow supersaturation in cirrus clouds (e.g. Gettelman *et al.*, 2010, Kuebbeler *et al.*, 2014), several do not. Predictions of ice cloud formation would benefit from a better understanding of the processes involved.

Our objective here is to analyze the parallel evolution in time of cirrus clouds and the surrounding water vapor, vertically resolved by a high-resolution ground-based lidar at La Réunion (20.9°S–55.5°E), in the subtropical upper troposphere where very few high-resolution observations have been collected so far. We focus on a 2-day case study and follow the methodology described by Comstock *et al.* (2004) – hereafter C04. Combining the lidar measurements (Section 2) with

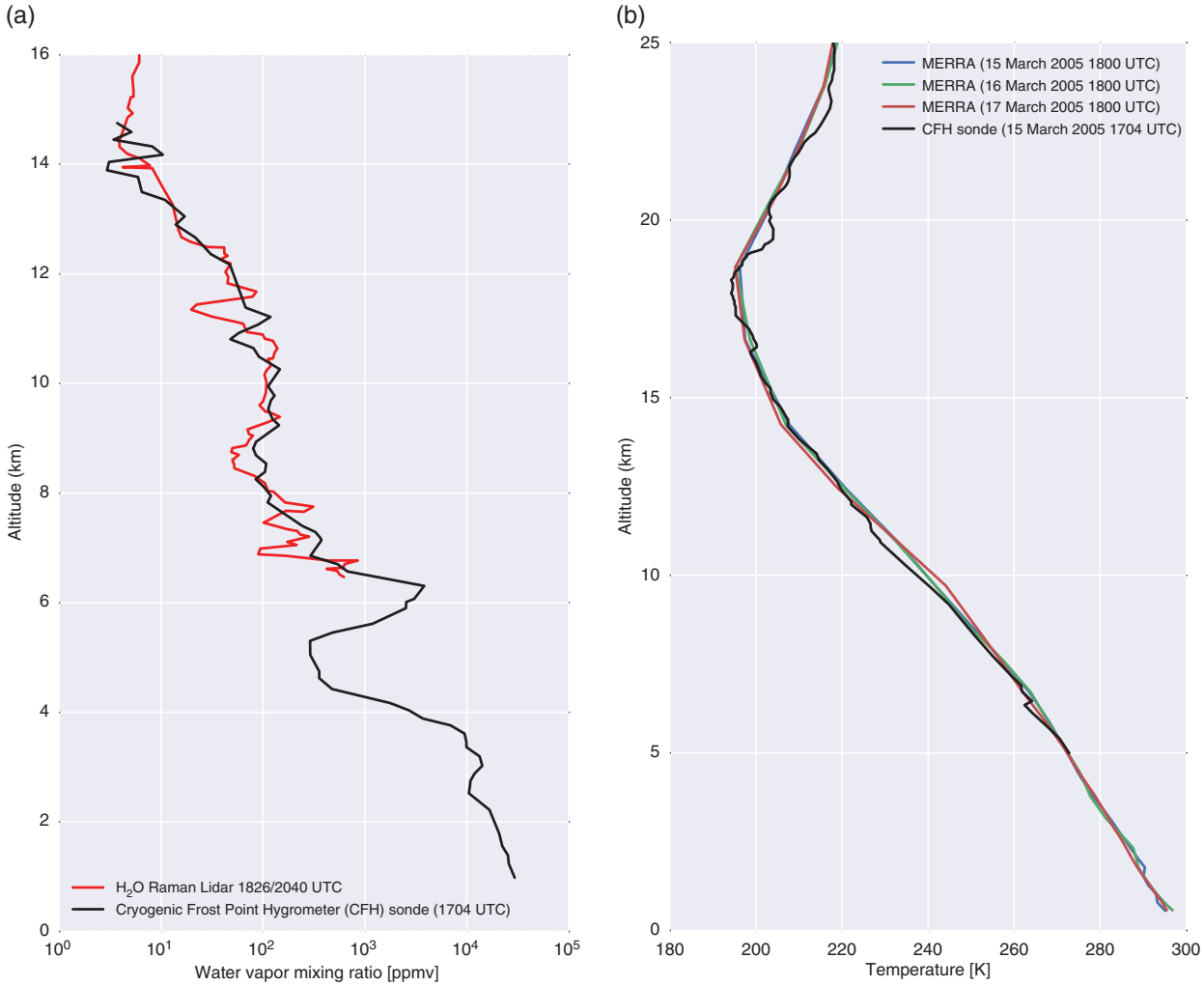

Figure 1. (a) Water vapor mixing ratio profile from RMR lidar (red) and Cryogenic Frost Point Hygrometer (CFH, black) on 15 March 2005. The CFH is used to calibrate the lidar water vapor mixing ratio profile (b). Temperature profile measured from the CFH radiosonde (black) during its descent starting at 1704 UTC on 15 March and from MERRA reanalysis at 1800 UTC (red) on 15, 16 and 17 March. On the 15th both temperature profiles agree within 1 K.

satellite observations, we examine ice supersaturation conditions within and around the cirrus clouds (Section 3). Section 4 provides a summary.

2. Lidar water vapor and cloud detection retrievals

The Rayleigh-Mie-Raman (RMR) lidar system was routinely operated at night (except in presence of low clouds) at the Observatoire de Physique de l'Atmosphère de la Réunion (OPAR) at 80 m ASL (Baray *et al.*, 2006). The instrument provides high-resolution profiles of water vapor relative concentration, while simultaneously detecting clouds (Hoareau *et al.*, 2012). Such measurements were acquired during nearly a hundred nights over the 2002–2005 period, with higher coverage in spring and autumn when masking by deep convection is less frequent (Cadet *et al.*, 2003). Hoareau *et al.* (2009) described the water vapor retrieval methodology. Our case study between 15 and 17 March 2005 presents a high quality of water vapor and cloud detection retrievals compared with the rest of the dataset.

The RMR lidar measures a vertical profile every 2 min, at 150-m resolution. To increase the signal-to-noise ratio and reduce the random error in water vapor retrievals, the data are smoothed temporally over 6 min, and averaged vertically using variable bin sizes, from 150 m near the ground to ~1 km in the upper troposphere. These tuned parameters, found by an iterative converging approach, lead to optimal night-time water vapor uncertainties between ~5% at 8 km and ~20% at 12–13 km.

The relative concentrations of water vapor retrieved from lidar need to be calibrated using absolute measurements. Here we used a Cryogenic Frost Point Hygrometer (CFH), launched on 15 March (Figure 1(a)). This radiosonde does not require calibration and can be considered an absolute reference for water vapor. Its uncertainty in frost point measurement is better than 0.5 K, leading in the Tropics to a mixing ratio uncertainty of ~4% in the lower troposphere to ~10% in the tropopause (Vömel *et al.*, 2007). As

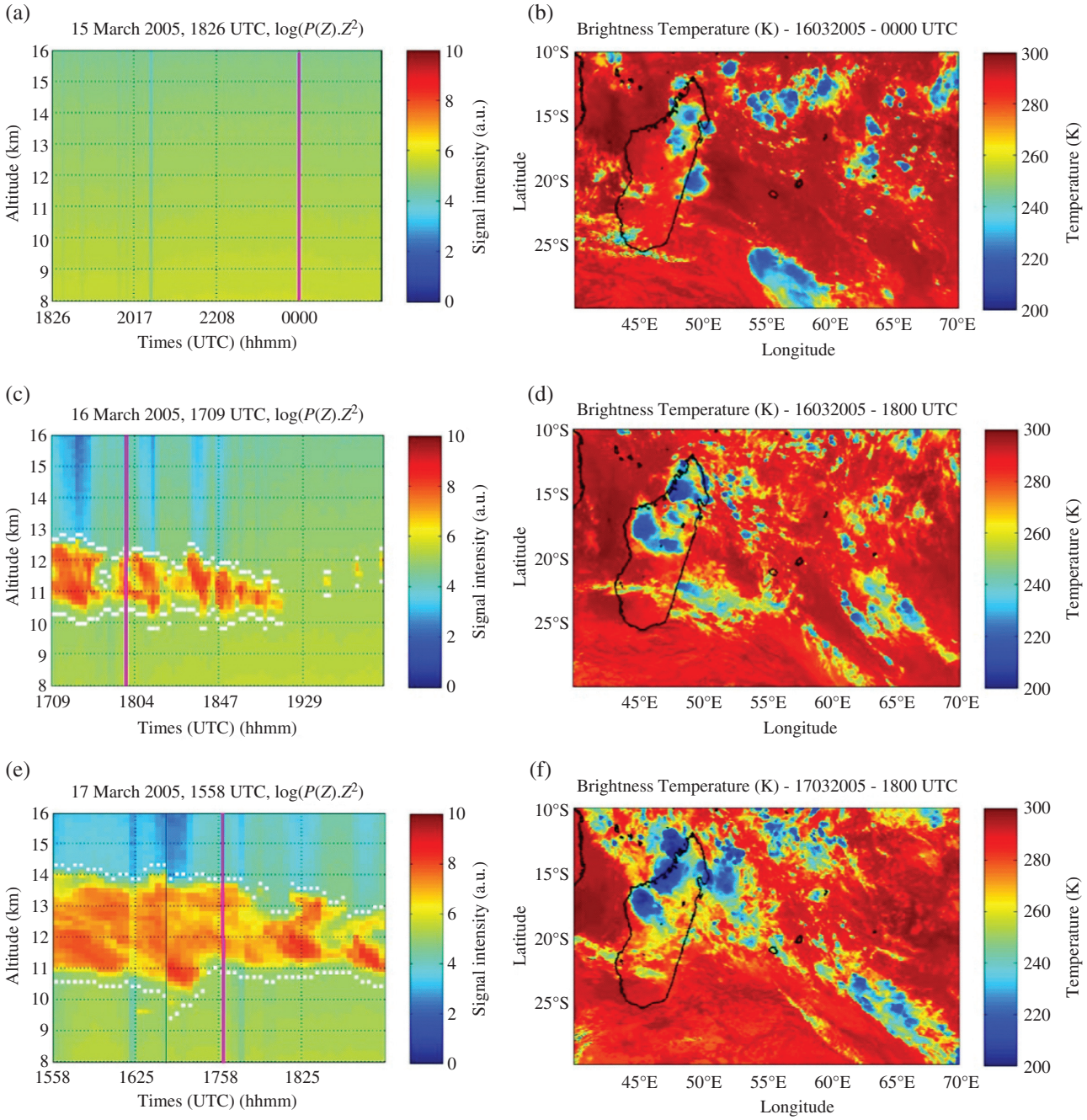

Figure 2. Observations during the 3-day case study: ground-based RMR range-corrected lidar signal intensity profiles (a, c, e) and brightness temperature images from merged geostationary satellites products, centered on La Reunion lidar (b, d, f). On lidar profiles, the cloud boundaries are shown as white squares, and the time of satellite observation shown as vertical pink lines.

the instrument configuration was not modified during the case study, we consider the calibration coefficient stable. The calibration coefficient was selected to minimize the difference between the lidar and CFH water vapor profiles at all altitude levels. Calibrated profiles in Figure 1(a) are in good agreement.

3. Case study

3.1. Cloud presence and history

Figure 2 shows observations for the 15–17 March case study: RMR lidar profiles on the left, and Brightness Temperature (BT) maps on the right. BT images are based on merged infrared measurements (peak frequencies from 10.7 to 11.5 μm) from geostationary satellites GMS, GOES-8 and 10, Meteosat-5 and 7, available at 4-km resolution between 60°S and 60°N (Janowiak *et al.*, 2001). On 15 March 2005 the lidar saw no cloud during its entire acquisition period, from 1825 to 0150 UTC (22:25 to 05:50 local time, Figure 2(a)). On 16 March, it probed a cirrus cloud from 1710 to 1920 UTC between 10 and 13 km (Figure 2(c)), and the next day from 1600 to 1850 UTC between 10 and 14 km (Figure 2(e)). We put cloud boundaries (white squares) where the measured signal is at least 3 times

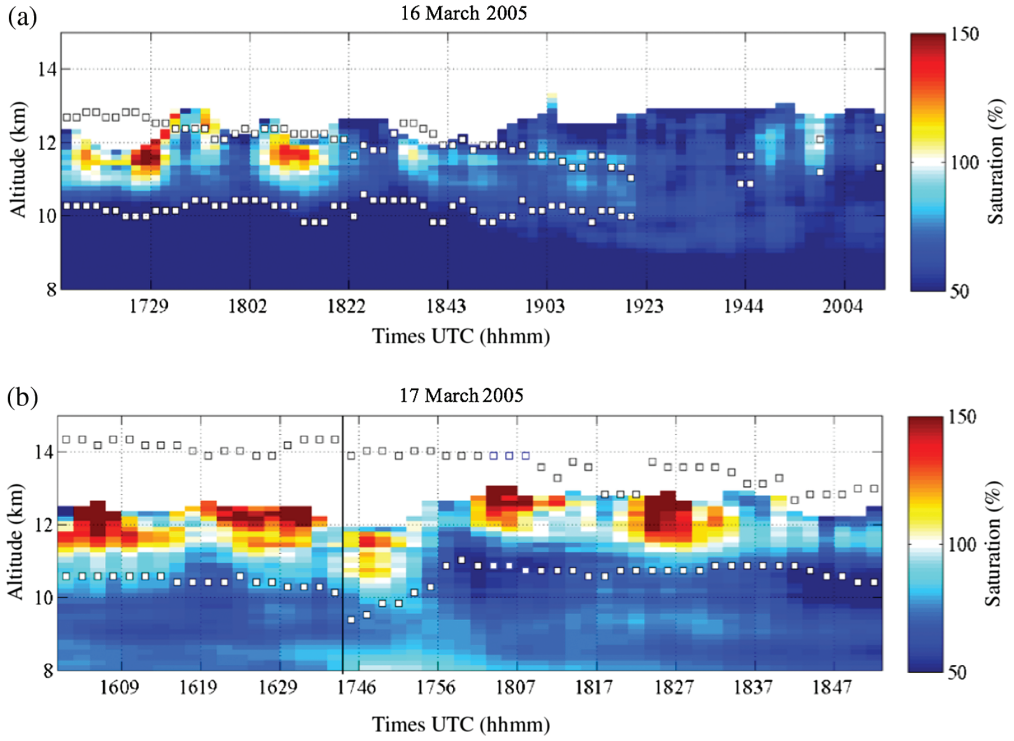

Figure 3. Vertical profiles of saturation over ice for the lidar acquisition time periods over the 2 cloudy days of the case study (16 March (a) and 17 March (b)). In white areas, the random error of water vapor mixing ratio is larger than 20% and saturation is not retrieved. Cloud boundaries are reported as white squares from Figure 2(c) and (e).

the expected clear-sky molecular signal. Additional BT imagery (Video S1, Supporting information) and back-trajectories using HYSPLIT (Draxler and Hess, 1998, not shown) suggest the cirrus clouds observed by the lidar on 16 and 17 March probably come from convective cells on the Eastern shore of Madagascar, ~700 km west of La Réunion. Convective activity started there between 19°S and 21°S at ~2100 UTC on 15 March, then developed while slightly drifting West until 0600 UTC on 16 March. The convective cells completely dissipated around 0800 UTC, while associated cirrus clouds drifted East, passed over La Réunion between 1400 and 2000 UTC, and finally dissipated. A similar scenario can be proposed for the cirrus observed on 17 March (Figure 2(e)), coming from a convective cell activated East of Madagascar on 16 March near 2000 UTC. This cell is more important and extensive than the one discussed above, and with numerous others along the Madagascar shore eventually led to a large area covered with cirrus clouds. On 17 March geostationary imagery shows clouds with BT<240 K over La Réunion continuously between 0800 and 2000 UTC. Changes in total column optical depths retrieved by the lidar (not shown) correlate well with BT changes over La Réunion from geostationary imagery, suggesting that both instruments observe the same clouds.

3.2. Water vapor

Using retrievals from the RMR lidar, we document the Relative Humidity with respect to ice (RHi) inside and around the observed cirrus cloud. Using profiles of water vapor mixing ratio together with temperature and pressure, we estimated the saturation over ice threshold (using the Sonntag, 1994 formulation). We completed the temperature and pressure record using MERRA reanalyses (Rienecker *et al.*, 2011) every 6 h on 72 vertical levels and a 0.75° grid. We selected data closest to the location and time of lidar observations for each date, and interpolated profiles at the times and heights of lidar retrievals. We considered the temperature profile constant over each lidar acquisition periods (always shorter than 6 hours). To exclude possible liquid particles driven by different nucleation/dissipation mechanisms, we only considered temperatures colder than −38 °C, where only ice is found (Cesana *et al.*, 2015). Comparing temperature profiles from the CFH (1704 UTC) and MERRA (1800 UTC) on 15 March (Figure 1(b)) shows an absolute difference below 1 °C (~0.35 °C ± 0.9 for the entire profile and 0.06 °C ± 1.2 for temperatures colder than −38 °C), consistent with Rienecker *et al.*, 2011. Since most of our water vapor measurements coincide with temperatures warmer than −60 °C, we think the temperature accuracy reasonable. Such uncertainties translate to RHi variances of ~11% at −38 °C and ~14% at −60 °C.

Figure 3 illustrates the evolution of RHi for 16 and 17 March when clouds were observed by the lidar. Saturation levels within clouds are correlated with their optical depth, which is limited on 16 March (<0.2) and larger on 17 March (up to 0.3). Cloud boundaries (white squares) are reported from Figure 2. As in C04, we stop retrievals when the random error of the water vapor mixing ratio (Section 2b in Hoareau *et al.*, 2009)

exceeds 20%. This leads to empty areas in the upper part of profiles. On 15 March (not shown), saturation stays below 50%, consistently with the reported absence of lidar cloud detection (Figure 2(a)). On 16 March (Figure 3(a)), RHi frequently exceeds 100% until 18:22, but falls below 100% within the whole cloud after 18:43 (evaporation stage) and dwindles almost to clear-sky levels (~60%). After 19:00, enhanced but unsaturated water vapor levels expand beyond the identified cloud boundaries. Saturation keeps falling and expanding after complete cloud dissipation (19:23 and beyond). On 17 March (Figure 3(b)), RHi rises to significant levels even in clear-sky (up to 80–90% below 10 km). Within the cloud, supersaturation remains strong for several hours over the entire observation period (consistent with Kärcher *et al.*, 2014 and the other studies mentioned previously).

Building on these retrievals, we follow again the lead of C04 and explore the RHi variability in the lowest 25% and middle 50% of its geometrical thickness (water vapor cannot be retrieved in the upper 25%, Figure 3). In the middle segment of clouds (Figure 4(a)), 34% of points are above ice saturation (RHi~96% on average), close to the 31% reported by C04 within cirrus clouds using a full year of observations. In the lowest segment, only 10% of points are above ice saturation (RHi~76% on average, up to 140%). We retrieve RHi as high as 200%, which sometimes show up in the literature but are inconsistent with accepted theory. Here they are probably due to unaccounted small-scale temperature fluctuations. Our results are consistent with previous studies of ice supersaturation in cirrus clouds using Raman lidar in North Hemisphere midlatitudes (C04, Comstock *et al.*, 2008). Their observation that supersaturation occurs more frequently near the top of cirrus clouds (regions of crystal growth or deposition) than near cloud base (where sedimentation or sublimation occurs) is applicable to our current case study of South Hemisphere tropical cirrus clouds.

Finally, we examine the variability of RHi (1) inside cirrus clouds, (2) in clear-sky points in cloudy profiles, and (3) in clear-sky points in clear-sky profiles (Figure 4(b)). Inside the cirrus, supersaturation occurs ~24% of the time, as already reported in Figure 4(a). In clear-sky profiles, we find supersaturation to be extremely rare, less than 1%. This is consistent with *in situ* measurements at Tropical, mid- and polar latitudes from Krämer *et al.*, 2009. Combining global-scale satellite remote sensing observations with *in situ* probe measurements, both Lamquin *et al.* (2012) and Smit *et al.* (2014) found limited but non-negligible supersaturation in supposedly clear-sky conditions, as did Spichtinger *et al.* (2004) from probes alone. However, the sensors used in these studies cannot detect clouds and the presence of clouds might bias those results. Clear-sky RHi are differently distributed in profiles that contain cloudy points at another altitude: clear-sky RHi is larger near a cloud. In this case study, it seems these higher RHi appear as water evaporates during cloud dissipation (on 16 March) or at altitudes too warm to trigger nucleation or deposition (below 10 km on 17 March).

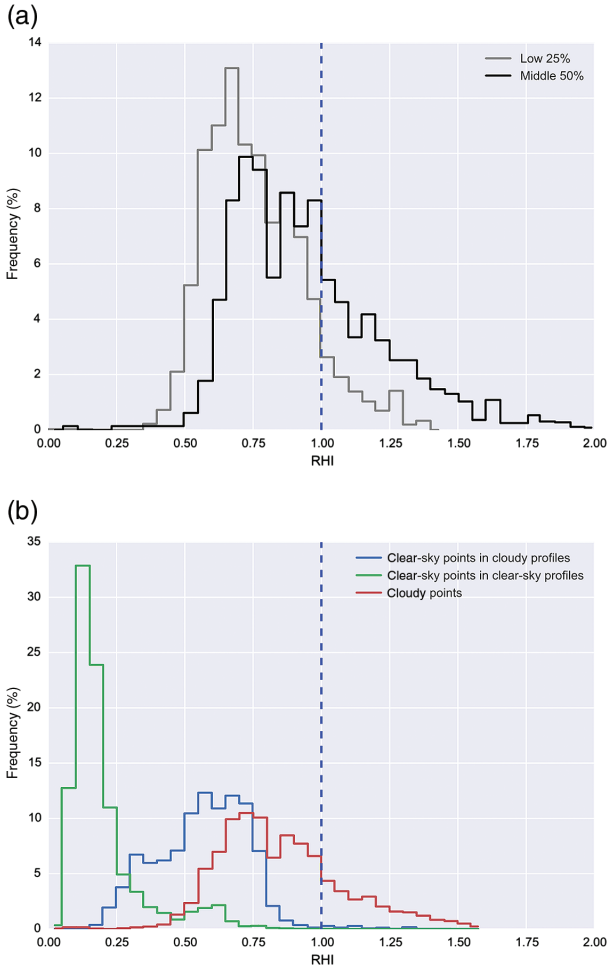

Figure 4. Distribution of saturation over ice derived from RMR lidar measurements in the lowest 25% and middle 50% of clouds (a), and in cloudy versus clear-sky points (b).

4. Conclusions

We evaluated water vapor saturation over ice within and around subtropical cirrus clouds, by combining profiles of temperature, pressure, cloud detection and water vapor mixing ratio observed from Raman lidar over La Réunion. We find that supersaturation occurs frequently within the observed cirrus clouds (25% of the time), and most frequently in the middle segment of clouds (34% of the time), in agreement with similar results in the North Hemisphere (C04). We could not document supersaturation near cloud top, where retrievals were cut off. Vertical profiles of water vapor from Raman lidar had not been documented within or near cirrus clouds in the Southern Hemisphere so far. We also find clear-sky air is more saturated with water vapor around cirrus clouds ($30\% < \mathrm{RHi} < 80\%$) than when clouds are totally absent ($\mathrm{RHi} < 30\%$). We never find supersaturation in low-level clear air regions, where our water vapor retrievals are most robust thanks to a strong lidar signal. One of the possible scenarios

that are not inconsistent with our observations is one of cloud formation at low supersaturations through heterogeneous freezing on aerosols acting as particularly efficient ice nuclei (e.g. mineral dust and/or metallic particles, Cziczo *et al.*, 2013). In such conditions, only a small number of ice crystals are created, offering a limited surface for water vapor deposition. This does not lower the water vapor concentration enough to reach subsaturation, leading to persistent in-cloud supersaturations. High-resolution mesoscale simulations (cf. Appendix S1, Supporting information) suggest that the observed supersaturation and clouds are probably due to the combined effects of advected water vapor brought to high altitudes by convection and small-scale temperature fluctuations created by high-tropospheric waves, especially on 16 March.

In the future, we hope to identify in the RMR record additional cases of high-quality water vapor and cloud measurements, and extend this study. Moreover, we plan to investigate how frequent are the cloud conditions we describe on a global scale using CALIOP data (Winker *et al.*, 2009), and extrapolate the global and seasonal frequency of the related ice supersaturation conditions we found associated. We also intend to use these findings to evaluate the capacity of mesoscale models to reproduce the observed cloud formation and water vapor variations.

Supporting information

The following supporting information is available:

Appendix S1. Observations of ice supersaturation inside and near cirrus clouds: a case study in the subtropics.

Video S1. Brightness temperature.

References

Baray J-L, Leveau J, Baldi S, Jouzel J, Keckhut P, Bergametti G, Ancellet G, Bencherif H, Cadet B, Carleer M, David C, De Maziere M, Faduilhe D, Godin Beekmann S, Goloub P, Goutail F, Metzger JM, Morel B, Pommereau JP, Porteneuve J, Portafaix T, Posny F, Robert L, Van Roozendael M. 2006. An instrumented station for the survey of ozone and climate change in the southern tropics: scientific motivation, technical description and future plans. *Journal of Environmental Monitoring* **8**: 1020–1028.

Cadet B, Goldfarb L, Faduilhe D, Baldy S, Giraud V, Keckhut P, Réchou A. 2003. A sub-tropical cirrus clouds climatology from Reunion Island (21°S, 55°E) lidar data set. *Geophysical Research Letters* **30**: 1130.

Cesana G, Chepfer H. 2012. How well do climate models simulate cloud vertical structure? A comparison between CALIPSO-GOCCP satellite observations and CMIP5 models. *Geophysical Research Letters* **39**: 20.

Cesana G, Waliser DE, Jiang X, Li J-LF. 2015. Multimodel evaluation of cloud phase transition using satellite and reanalysis data. *Journal of Geophysical Research* **120**(15): 7871–7892, doi: 10.1002/2014JD022932.

Comstock JM, Ackerman TP, Turner DD. 2004. Evidence of high ice supersaturation in cirrus clouds using ARM Raman lidar measurements. *Geophysical Research Letters* **31**(11), doi: 10.1029/2004GL019705.

Comstock JM, Lin R-F, Starr DO, Yang P. 2008. Understanding ice supersaturation, particle growth, and number concentration in cirrus clouds. *Journal of Geophysical Research* **113**(D23): D23211–D23220.

Cziczo DJ, Froyd KD, Hoose C, Jensen EJ, Diao M, Zondlo MA, Smith JB, Twohy CH, Murphy DM. 2013. Clarifying the dominant sources and mechanisms of cirrus cloud formation. *Science* **340**(6138): 1320–1324.

Delanoë J, Hogan RJ, Forbes RM, Bodas-Salcedo A, Stein THM. 2011. Evaluation of ice cloud representation in the ECMWF and UK Met Office models using CloudSat and CALIPSO data. *Quarterly Journal of the Royal Meteorological Society* **137**(661): 2064–2078.

Dinh T, Fueglistaler S. 2014. Microphysical, radiative and dynamical impacts of thin cirrus clouds on humidity in the tropical tropopause layer and stratosphere. *Geophysical Research Letters* **41**: 6949–6955.

Draxler RR, Hess GD. 1998. An overview of the HYSPLIT_4 modeling system of trajectories, dispersion, and deposition. *Australian Meteorological Magazine* **47**: 295–308.

Gayet J-F, Ovarlez J, Shcherbakov VN, Ström J, Schumann U, Minikin A, Auriol F, Petzold A, Monier M. 2004. Cirrus cloud microphysical and optical properties at southern and northern midlatitudes during the INCA experiment. *Journal of Geophysical Research* **109**(D20): D20206.

Gettelman A, Liu X, Ghan SJ, Morrison H, Park S, Conley AJ, Klein SA, Boyle J, Mitchell DL, Li J-LF. 2010. Global simulations of ice nucleation and ice supersaturation with an improved cloud scheme in the Community Atmosphere Model. *Journal of Geophysical Research* **115**(D18): D18216.

Heintzenberg J, Charlson RJ. 2009. *Clouds in the Perturbed Climate System; Their Relationship to Energy Balance, Atmospheric Dynamics, and Precipitation*. MIT Press: Cambridge, MA; 597 pp.

Hoareau C, Keckhut P, Sarkissian A, Baray JL, Durry G. 2009. Methodology for water monitoring in the upper troposphere with Raman Lidar at the Haute-Provence observatory. *Journal of Atmospheric and Oceanic Technology* **26**(10): 2149–2160.

Hoareau C, Keckhut P, Baray J-L, Robert L, Courcoux Y, Porteneuve J, Vömel H, Morel B. 2012. A Raman lidar at La Reunion (20.8°S, 55.5°E) for monitoring water vapour and cirrus distributions in the subtropical upper troposphere: preliminary analyses and description of a future system. *Atmospheric Measurement Techniques* **5**: 1333–1348.

Janowiak JE, Joyce RJ, Yarosh Y. 2001. A real-time global half-hourly pixel-resolution infrared dataset and its applications. *Bulletin of the American Meteorological Society* **82**: 205–218.

Jensen EJ, Diskin G, Lawson RP, Lance S, Bui TP, Hlavka D, McGill M, Pfister L, Toon OB, Gao R. 2013. Ice nucleation and dehydration in the Tropical Tropopause Layer. *Proceedings of the National academy of Sciences of the United States of America* **110**(6): 2041–2046.

Kärcher B, Burkhardt U. 2008. A cirrus cloud scheme for general circulation models. *Quarterly Journal of the Royal Meteorological Society* **134**: 1439–1461.

Kärcher B, Dornbrack A, Solch I. 2014. Supersaturation variability and cirrus ice crystal size distributions. *Journal of the Atmospheric Sciences* **71**(8): 2905–2926.

Krämer M, Schiller C, Afchine A, Bauer R, Gensch I, Mangold A, Schlicht S, Spelten N, Sitnikov N, Borrmann S, de Reus M, Spichtinger P. 2009. Ice supersaturations and cirrus cloud crystal numbers. *Atmospheric Chemistry and Physics* **9**: 3505–3522.

Kuebbeler M, Lohmann U, Hendricks J, Karcher B. 2014. Dust ice nuclei effects on cirrus clouds. *Atmospheric Chemistry and Physics* **14**(6): 3027–3046.

Lamquin N, Gierens K, Stubenrauch CJ, Chatterjee R. 2009. Evaluation of upper tropospheric humidity forecasts from ECMWF using AIRS and CALIPSO data. *Atmospheric Chemistry and Physics* **9**: 1779–1793.

Lamquin N, Stubenrauch CJ, Gierens KM, Burkhardt U, Smit H. 2012. A global climatology of upper-tropospheric ice supersaturation occurrence inferred from the Atmospheric Infrared Sounder calibrated by MOZAIC. *Atmospheric Chemistry and Physics* **12**(1): 381–405.

Martins E, Noel V, Chepfer H. 2011. Properties of cirrus and subvisible cirrus from nighttime CALIOP, related to atmospheric dynamics and water vapor. *Journal of Geophysical Research* **116**: D02208.

Nam CCW, Quaas J. 2012. Evaluation of clouds and precipitation in the ECHAM5 general circulation model using CALIPSO and CloudSat satellite data. *Journal of Climate* **25**(14): 4975–4992.

Reverdy M, Noel V, Chepfer H, Legras B. 2012. On the origins of subvisible cirrus clouds in the tropical upper troposphere. *Atmospheric Chemistry and Physics* **12**: 12081–12101.

Rienecker MM, Suarez MJ, Gelaro R, Todling R, Bacmeister J, Liu E, Bosilovich MG, Schubert SD, Takacs L, Kim G-K, Bloom S, Chen J, Collins D, Conaty A, da Silva A, Gu W, Joiner J, Koster RD, Lucchesi R, Molod A, Owens T, Pawson S, Pegion P, Redder CR, Reichle R, Robertson FR, Ruddick AG, Sienkiewicz M, Woollen J. 2011. MERRA: NASA's modern-era retrospective analysis for research and applications. *Journal of Climate* **24**: 3624–3648.

Ringer MA, McAvaney BJ, Andronova N, Buja LE, Esch M, Ingram WJ, Li B, Quaas J, Roeckner E, Senior CA, Soden BJ, Volodin EM, Webb MJ, Williams KD. 2006. Global mean cloud feedbacks in idealized climate change experiments. *Geophysical Research Letters* **33**: L07718.

Sandor B, Jensen EJ, Stone E, Read W, Waters J, Mergenthaler J. 2000. Upper tropospheric humidity and thin cirrus. *Geophysical Research Letters* **27**(17): 2645–2648.

Smit HGJ, Rohs S, Neis P, Boulanger D, Krämer M, Wahner A, Petzold A. 2014. Technical Note: reanalysis of upper troposphere humidity data from the MOZAIC programme for the period 1994 to 2009. *Atmospheric Chemistry and Physics* **14**(23): 13241–13255.

Sonntag D. 1994. Advancements in the field of hygrometry. *Meteorologische Zeitschrift N. F.* **3**: 51–66.

Spichtinger P, Cziczo DJ. 2010. Impact of heterogeneous ice nuclei on homogeneous freezing events in cirrus clouds. *Journal of Geophysical Research* **115**(D14): D14208–D14222.

Spichtinger P, Gierens K. 2009. Modelling of cirrus clouds. Part 2: competition of different nucleation mechanisms. *Atmospheric Chemistry and Physics* **9**: 2319–2334.

Spichtinger P, Gierens K, Smith GJ, Ovarlez J, Gayet J-F. 2004. On the distribution of relative humidity in cirrus clouds. *Atmospheric Chemistry and Physics* **4**(3): 639–647.

Su H, Ziang JH, Stephens GL, Vane DG, Livesey NJ. 2009. Radiative effects of upper tropospheric clouds observed by Aura MLS and CloudSAT. *Geophysical Research Letters* **36**: L09815.

Vömel H, Barnes JE, Forno RN, Fujiwara M, Hasebe F, Iwasaki S, Kivi R, Komala N, Kyro E, Leblanc T, Morel B, Ogino SY, Read WG, Ryan SC, Saraspriya S, Selkirk H, Shiotani M, Valverde Canossa J, Whiteman DN. 2007. Validation of aura microwave limb sounder water vapour by balloon-borne cryogenic frost point hygrometer measurements. *Journal of Geophysical Research* **112**: DS24S37.

Winker D, Vaughan MA, Omar A, Hu Y, Powell KA. 2009. Overview of the CALIPSO mission and CALIOP data processing algorithms. *Journal of Atmospheric and Oceanic Technology* **26**: 2310–2323.

Zhang MH, Lin WY, Klein SA, Bacmeister JT, Bony S, Cederwall RT, DelGenio AD, Hack JJ, Loeb NG, Lohmann U, Minnis P, Musat I, Pincus R, Stier P, Suarez MJ, Webb MJ, Wu JB, Xie SC, Yao M-S, Zhang JH. 2005. Comparing clouds and their seasonal variations in 10 atmospheric general circulation models with satellite measurements. *Journal of Geophysical Research* **110**: D15S02.